Anisotropy in cohesive, frictional Granular Media

Stefan Luding† ‡

† Particle Technology, DelftChemTech, TUDelft, Julianalaan 136, 2628 BL Delft, The Netherlands

Abstract.

The modeling of cohesive, frictional granular materials with a discrete particle molecular dynamics is reviewed. From the structure of the quasi-static granular solid, the fabric, the stress- and the stiffness tensors are determined, including both normal and tangential forces. The influence of the material properties on the flow behavior is also reported, including relations between the microscopic attractive force and the macroscopic cohesion as well as the dependence of the macroscopic friction on the microscopic contact friction coefficient. Related to the dynamics, the anisotropy of both structure and stress are exponentially approaching the maximum.

1. Introduction

The microscopic understanding of the macroscopic material behavior of granular materials like sand or powder is one of todays great challenges in material science and physics. Granular media are discontinuous, inhomogeneous, disordered, and anisotropic, on a "microscopic" scale and their behavior is usually intermittent, non-linear and history dependent. Nevertheless, continuum models are applied in large scale industrial design of, e.g., silos, where the models are based on constitutive relations and often on experimental observations and empirical assumptions.

The rich phenomenology observed in granular matter is due to the changing contact network of the structure formed by the grains, but also due to the inhomogeneous stress distribution in granular assemblies and the corresponding force-networks. There are always large fluctuations of contact forces and a reorganization of the network due to deformations typically leads to a re-structuring of those. When an initially isotropic contact network is deformed, the result is likely to be anisotropic. Translating this "microscopic" information all the way up to a macroscopic description, via a so-called micro-macro model, is one issue of this paper.

We do not review all the existing literature in this field here, rather we point the readers attention to the books by [1–3] and some references by various groups [4–14] and the references therein. Part of the results presented here was already published in Refs. [10, 14, 15] In the following, a micro-macro averaging formalism is presented, based on single contact information [14], and the numerical method of molecular dynamics (MD),

‡ *e-mail:* `s.luding@tnw.tudelft.nl`

also called discrete element method (DEM), see e.g. [7, 14–16], is applied in order to obtain the macroscopic constitutive relations. The behavior of the stress-, fabric- and stiffness-tensors under shear is discussed for different microscopic material parameters.

2. Simulation Details

The discrete element model (DEM) [1, 2, 7, 16–21] is briefly introduced in this section, for more details see the papers [10, 14, 15, 22–24] and the references therein. However, before going into numerical details, the model system is described.

2.1. Discrete Particle Model

The elementary units of granular materials are mesoscopic grains which deform under stress. Since the realistic modeling of the deformations of the particles is much too complicated, we relate the normal interaction force to the overlap δ of two circular particles, see Fig. 1.

If all forces $\boldsymbol{f}_i$ acting on the particle i, either from other particles, from boundaries or from external forces, are known, the problem is reduced to the integration of Newton's equations of motion for the translational and rotational degrees of freedom

$$m_i \frac{\mathrm{d}^2}{\mathrm{d}t^2} \boldsymbol{r}_i = \boldsymbol{f}_i \ , \quad \text{and} \quad I_i \frac{\mathrm{d}^2}{\mathrm{d}t^2} \boldsymbol{\varphi}_i = \boldsymbol{t}_i \tag{1}$$

with the mass m_i of particle i, its position $\boldsymbol{r}_i$ the total force $\boldsymbol{f}_i = \sum_c \boldsymbol{f}_i^c$ acting on it due to contacts with other particles or with the walls, its moment of inertia I_i, its angular velocity $\boldsymbol{\omega}_i = \mathrm{d}\boldsymbol{\varphi}_i/\mathrm{d}t$ and the total torque $\boldsymbol{t}_i = \sum_c \boldsymbol{l}_i^c \times \boldsymbol{f}_i^c$.

2.1.1. Linear normal contact law

Two particles i and j interact only if they are in contact so that their overlap,

$$\delta = (a_i + a_j) - (\boldsymbol{r}_i - \boldsymbol{r}_j) \cdot \boldsymbol{n} \ , \tag{2}$$

is positive, with the unit vector $\boldsymbol{n} = \boldsymbol{n}_{ij} = (\boldsymbol{r}_i - \boldsymbol{r}_j)/|\boldsymbol{r}_i - \boldsymbol{r}_j|$ pointing from j to i.

The force on particle i, from particle j can be decomposed into a normal and a tangential part, where the simplest normal force is a linear spring and a linear dashpot

$$f_i^n = k\delta + \gamma_0 \dot{\delta} \ , \tag{3}$$

with spring constant k and some damping coefficient γ_0. The half-period of a vibration around the equilibrium position can be computed, and one obtains a typical response time $t_c = \pi/\omega$, with $\omega = \sqrt{(k/m_{ij}) - \eta_0^2}$, the eigenfrequency of the contact, the reduced mass $m_{ij} = m_i m_j/(m_i + m_j)$, and the rescaled damping coefficient $\eta_0 = \gamma_0/(2m_{ij})$. The energy dissipation during a collision, as caused by the dashpot, leads to a restitution coefficient $r = -v_n'/v_n = \exp(-\eta_0 t_c)$, where the prime denotes the normal velocity after a collision. For a more detailed discussion of this and other, more realistic, non-linear contact models see e.g. [15, 25].

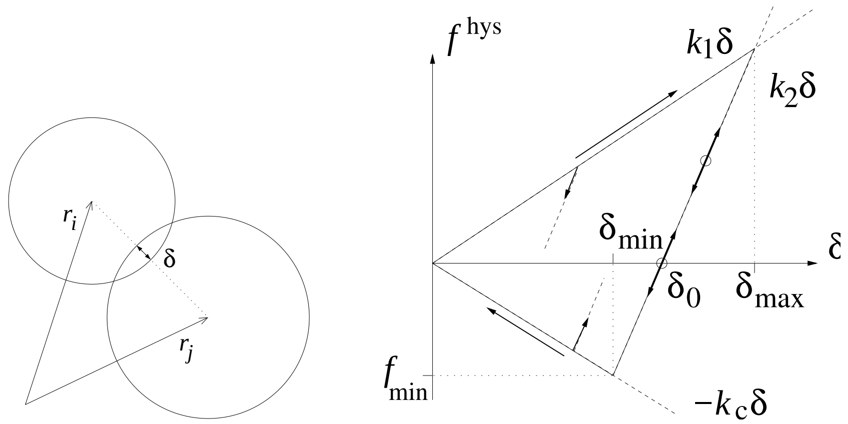

Figure 1. (Left) Two particle contact with overlap δ. (Right) Force displacement relation with three material parameters k_1, k_2, and k_c.

The contact duration t_c is also of practical technical importance, since the integration of the equations of motion is stable only if the integration time-step Δt_{MD} is much smaller than t_c. Since t_c depends on the magnitude of dissipation, in the extreme case of an overdamped spring, it can become very large. Therefore, the use of neither too weak nor too strong dissipation is recommended.

2.1.2. Cohesive (Hysteretic) Normal Contact Model

Here we apply a variant of the linear hysteretic spring model [15, 22, 25–27], as an alternative to the frequently applied spring-dashpot models. This model is the simplest version of some more complicated nonlinear-hysteretic force laws [26, 28, 29], which reflect the fact that at the contact point, plastic deformations may take place. The repulsive (hysteretic) force can be written as

$$f^{\text{hys}} = \begin{cases} k_1\delta & \text{for loading,} \qquad \text{if } k_2(\delta-\delta_0) \geq k_1\delta \\ k_2(\delta-\delta_0) & \text{for un/reloading,} \quad \text{if } k_1\delta > k_2(\delta-\delta_0) > -k_c\delta \\ -k_c\delta & \text{for unloading,} \qquad \text{if } -k_c\delta \geq k_2(\delta-\delta_0) \end{cases} \tag{4}$$

with $k_1 \leq k_2$, see Fig. 1.

During the initial loading the force increases linearly with the overlap δ, until the maximum overlap δ_{max} is reached (which has to be kept in memory as a history parameter). The line with slope k_1 thus defines the maximum force possible for a given δ. During unloading the force drops from its value at δ_{max} down to zero at overlap $\delta_0 = (1 - k_1/k_2)\delta_{\text{max}}$, on the line with slope k_2. Reloading at any instant leads to an increase of the force along this line, until the maximum force is reached; for still increasing δ, the force follows again the line with slope k_1 and δ_{max} has to be adjusted accordingly.

Unloading below δ_0 leads to negative, attractive forces until the minimum force $-k_c\delta_{\text{min}}$ is reached at the overlap $\delta_{\text{min}} = (k_2 - k_1)\delta_{\text{max}}/(k_2 + k_c)$. This minimum force, i.e. the maximum attractive force, is obtained as a function of the model parameters

k_1, k_2, k_c, and the history parameter $\delta_{\rm max}$. Further unloading leads to attractive forces $f^{\rm hys} = -k_c\delta$ on the cohesive branch with slope $-k_c$. The highest possible attractive force, for given k_1 and k_2, is reached for $k_c \to \infty$, so that $f^{\rm hys}_{\rm max} = -(k_2 - k_1)\delta_{\rm max}$. Since this would lead to a discontinuity at $\delta = 0$, it is avoided by using finite k_c.

The lines with slope k_1 and $-k_c$ define the range of possible force values and departure from these lines takes place in the case of unloading and reloading, respectively. Between these two extremes, unloading and reloading follow the same line with slope k_2. Possible equilibrium states are indicated as circles in Fig. 1, where the upper and lower circle correspond to a pre-stressed and stress-free state, respectively. Small perturbations lead, in general, to small deviations along the line with slope k_2 as indicated by the arrows.

A non-linear un/reloading behavior would be more realistic, however, due to a lack of detailed experimental informations, we use the piece-wise linear model as a compromise. One refinement is a k_2 value dependent on the maximum overlap that implies small and large plastic deformations for weak and strong contact forces, respectively. One model, as implemented recently [15, 23], requires an additional model parameter, $\delta^*_{\rm max}$, so that $k_2(\delta_{\rm max})$ is increasing from k_1 to k_2 (linear interpolation) with the maximum overlap, until $\delta^*_{\rm max}$ is reached §:

$$k_2(\delta_{\rm max}) = \begin{cases} k_2 & \text{if } \delta_{\rm max} \ge \delta^*_{\rm max} \\ k_{10} + (k_2 - k_1)\delta_{\rm max}/\delta^*_{\rm max} & \text{if } \delta_{\rm max} < \delta^*_{\rm max} \ , \end{cases} \tag{5}$$

with the stiffness for small overlaps k_{10}, that can be chosen in the range $k_1 \le k_{10} \le k_2$. (For the simulations presented below, $k_{10} = k_2$ was used; a detailed parameter study is far from the scope of this paper).

While in the case of collisions of particles with large deformations, dissipation takes place due to the hysteretic nature of the force-law, stronger dissipation of small amplitude deformations is achieved by adding the viscous, velocity dependent dissipative force from the linear contact law to the hysteretic force, such that $f^n = f^{\rm hys} + \gamma_0 v_n$. The hysteretic model contains the linear contact model as special case $k_1 = k_2 = k$.

2.1.3. Tangential Contact Model

The force in tangential direction is implemented in the spirit of Ref. [17], where a tangential spring was introduced, in order to account for static friction. Various authors have used this idea and numerous variants were implemented, see [30] for a summary and discussion. Since we use a special implementation, which can be used for dimensions $D = 2$ and $D = 3$ alike, it is necessary to repeat the model and define the implementation. In the static case, the tangential force is coupled to the normal force via Coulombs law, i.e. $f^t \le \mu^s f^n$, where for the sliding case one has dynamic friction with $f^t = \mu^d f^n$. The dynamic and the static friction coefficients follow, in general, the relation $\mu^d \le \mu^s$. However, for the following simulations we will apply $\mu = \mu^d = \mu^s$.

§ A limit to the slope k_2 is needed for practical reasons. If k_2 would not be limited, the contact duration could become very small so that the time step would have to be reduced below reasonable values.

(The first few simulations performed with $\mu^d \neq \mu^s$ do not allow for an insight into the relevance of a difference of the static and dynamic friction coefficients.) The static case requires an elastic spring, related to the tangential displacement, in order to allow for a static restoring force, i.e. a non-zero tangential force in static equilibrium due to activated Coulomb friction.

If a contact exists with non-zero normal force, the tangential force is active too, and we project the tangential spring into the actual tangential plane (this is necessary, since the frame of reference of the contact may have rotated since the last time-step)

$$\boldsymbol{\xi} = \boldsymbol{\xi}' - \boldsymbol{n}(\boldsymbol{n} \cdot \boldsymbol{\xi}') \ , \tag{6}$$

where $\boldsymbol{\xi}'$ is the old spring from the last iteration, and $\boldsymbol{n}$ is the normal unit vector. This action is relevant only for an already existing spring; if the spring is new, the tangential spring-length is zero anyway, however, its change/evolution is well defined below. The tangential velocity is

$$\boldsymbol{v}_t = \boldsymbol{v}_{ij} - \boldsymbol{n}(\boldsymbol{n} \cdot \boldsymbol{v}_{ij}) \ , \tag{7}$$

with the total relative velocity

$$\boldsymbol{v}_{ij} = \boldsymbol{v}_i - \boldsymbol{v}_j + a_i \boldsymbol{n} \times \boldsymbol{\omega}_i + a_j \boldsymbol{n} \times \boldsymbol{\omega}_j \ , \tag{8}$$

of the surfaces of the two contacting particles. Next, we calculate the tangential test-force as the sum of the tangential spring and a tangential viscous force (in analogy to the normal viscous force)

$$\boldsymbol{f}^t_{\mathrm{o}} = -k_t \, \boldsymbol{\xi} - \gamma_t \boldsymbol{v}_t \ , \tag{9}$$

with the tangential spring stiffness k_t and a tangential dissipation parameter γ_t.

Typically, a contact starts with finite tangential velocity and $\boldsymbol{\xi} = 0$; during the first time-steps, the velocity decreases and the spring is stretched. As long as $|\boldsymbol{f}^t_{\mathrm{o}}| \leq f^s_C$, with $f^s_C = \mu^s f^n$, one has the *static friction* case (1) and, on the other hand, if $|\boldsymbol{f}^t_{\mathrm{o}}|$ becomes larger than f^s_C, the sliding, *dynamic friction* case (2) is active with the (possibly lower) Coulomb limit $f^d_C = \mu^d f^n$. Sliding case (2) is active as long as, in the next steps, the test force remains $|\boldsymbol{f}^t_{\mathrm{o}}| > f^d_C$. If the tangential force drops below the dynamic Coulomb limit, $|\boldsymbol{f}^t_{\mathrm{o}}| \leq f^d_C$, static friction becomes active again, with the (possibly larger) Coulomb limit f^s_C, giving rise to stick-slip behavior.
In the former, *static* case (1), the tangential spring is incremented

$$\boldsymbol{\xi}' = \boldsymbol{\xi} + \boldsymbol{v}_t \, \delta t_{\mathrm{MD}} \ , \tag{10}$$

with the time step δt_{MD} of the DEM simulation. The new value of $\boldsymbol{\xi}'$ is to be used in the next iteration in Eq. (6), and the tangential force $\boldsymbol{f}^t = \boldsymbol{f}^t_{\mathrm{o}}$ as defined in Eq. (9) is used. In the latter, *sliding* case (2), the tangential spring is adjusted to a length which is consistent with Coulombs condition,

$$\boldsymbol{\xi}' = -\frac{1}{k_t} \left(f^d_C \, \boldsymbol{t} + \gamma_t \boldsymbol{v}_t \right) \ , \tag{11}$$

with the tangential unit vector, $\boldsymbol{t} = \boldsymbol{f}^t_{\mathrm{o}} / |\boldsymbol{f}^t_{\mathrm{o}}|$, defined by the direction of the force in Eq. (9), and thus the magnitude of the Coulomb limit is used. Inserting $\boldsymbol{\xi}'$ into Eq. (9)

leads to $\boldsymbol{f}_{\rm o}^t \approx f_C^d \boldsymbol{t}$. Note that $\boldsymbol{f}_{\rm o}^t$ and $\boldsymbol{v}_t$ are not necessarily parallel in three dimensions. However, the mapping in Eq. (11) works always, rotating the new spring such that the direction of the frictional force is unchanged and, at the same time, limiting the spring in length according to Coulombs law. In short notation the tangential force on particle i reads

$$\boldsymbol{f}_i^t = +\min\left(f_C, |\boldsymbol{f}_{\rm o}^t|\right) \boldsymbol{t} \ , \tag{12}$$

where f_C follows the selection rules described above.

Note that the tangential force described above is identical to the classical Cundall-Strack spring only in the limits $\mu = \mu^s = \mu^d$ and $\gamma_t = 0$. The sequence of computations and the definitions and mappings into the tangential direction, however, is new to our knowledge in so far that it accounts for different static and dynamic friction coefficients and can be easily generalized to three dimensions.

2.1.4. Background Friction

Note that the viscous dissipation takes place in a two-particle contact. In the bulk material, where many particles are in contact with each other, dissipation is very inefficient due to long-wavelength cooperative modes of motion [31, 32]. Therefore, an artificial background is introduced, so that the total force on particle i is

$$\boldsymbol{f}_i = \sum_c \left(f_i^n \hat{\boldsymbol{n}} + \boldsymbol{f}_i^t\right) - \gamma_{\rm b} \boldsymbol{v}_i \ , \tag{13}$$

with a viscous background damping constant $\gamma_{\rm b}$ for a rapid equilibration.

2.1.5. Other Forces

Other forces than those mentioned above, like long-range forces (electrostatic or van der Waals), contact couples, rolling- or torsion-friction are neglected in this study as well as a possible non-spherical shape of the particles. Research in this direction is in progress, however.

2.2. Model System

The "experiment" chosen is the biaxial box set-up, see Fig. 2, where the left and bottom walls are fixed. The right side-wall is subject to a constant stress, and the top-wall follows a pre-defined strain-path [10, 14]. In a typical "experiment", the top wall is smoothly and slowly shifted downward (according to a half cosine function), in order to avoid shocks and inertia effects, respectively. The right wall has a mass, $m_{\rm w}$, and moves stress controlled, dependent on the force $F(t)$ exerted on it by the material in the box and by a dashpot that damps its motion.

2.3. Parameters

The system examined in the following contains $N = 1950$ particles with radii a_i randomly drawn from a homogeneous distribution between $a_{\rm min} = 0.5\,10^{-3}\,$m and

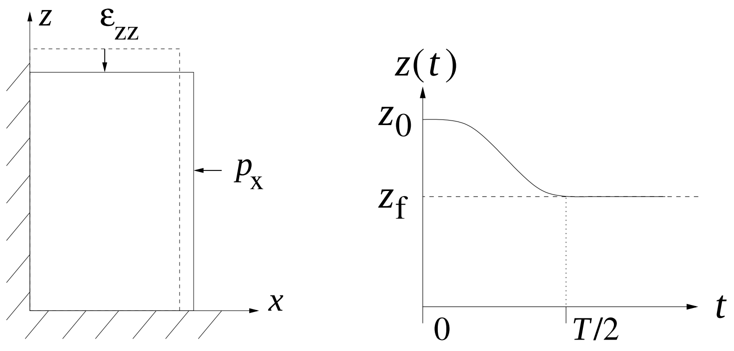

Figure 2. (Left) Schematic drawing of the model system. (Right) Position of the top-wall as function of time for the strain-controlled situation.

$a_{\max} = 1.5\,10^{-3}\,\mathrm{m}$. The masses of the cylindrical particles with height $h = 2.0\,10^{-4}\,\mathrm{m}$ are $m_i = \rho\pi h a_i^2$, with the density $\rho = 2.0\,10^3\mathrm{kg\,m^{-3}}$. The total mass of the particles in the system is thus $M \approx 0.0026\,\mathrm{kg}$ with the typical reduced mass of a pair of particles with mean radius, $m_{12} \approx 0.67\,10^{-6}\,\mathrm{kg}$. The wall properties are $m_{\mathrm{w}} = 10^{-4}\,\mathrm{kg}$ and $\gamma_{\mathrm{w}} = 2\,\mathrm{kg\,s^{-1}}$. If not explicitly mentioned, the material parameters are $k_1 = k_2/2$, $k_2 = 10^5\,\mathrm{N\,m^{-1}}$, $\gamma_0 = \gamma_t = 0.02\,\mathrm{kg\,s^{-1}}$, and $\gamma_{\mathrm{b}} = 10^{-5}\,\mathrm{kg\,s^{-1}}$, $\mu = 0.5$, and $k_t/k = 0.2$. This leads to a typical contact duration $t_c = 0.82\,10^{-5}\,\mathrm{s}$ and a restitution coefficient of $r = 0.89$, with the integration time-step used $\delta t_{MD} = 0.2\,10^{-6}\,\mathrm{s}$. The choice of parameters is rather arbitrary (with respect to the linear force model with the rather small stiffness), however, the finding below that the stiffness tensor scales with the spring constant rectifies it a-posteriori, i.e. the results do not depend on the stiffness explicitly. Additional simulations (not shown here) also confirm this statement. Note that the choice of the stiffness and a possible non-linear force law is more important for dynamic systems for, e.g., sound propagation than for the quasi-static system presented here.

2.4. Initial configuration

Initially, the particles are randomly distributed in a huge box, with rather low overall density and friction as well as cohesion are switched off. Then the box is compressed with isotropic pressure $p = p_{\mathrm{x}} = p_{\mathrm{z}}$, in order to achieve an initial condition as isotropic as feasible; there is remaining anisotropy of the order of a few per-cent in some situations, however. The configuration is relaxed until the kinetic energy is several orders of magnitude smaller than the potential contact energy. Starting from this relaxed, overconsolidated, isotropic initial configuration, the strain is applied to the top wall and the response of the system is examined with friction and cohesion active.

3. Averaging and micro-macro transition

In order to obtain macroscopic quantities, averages are taken over single-contact elementary tensors, as derived in [14]. Note that we focus here on those quantities that can be obtained from static snapshots and do not rely on (real) displacements, see [14, 15, 33] for more details. The simplest averaging approach is used here, i.e. a contact is taken into account if the corresponding particle center lies within the averaging volume (alternatives are discussed in [14]). This corresponds to a pre-averaging over single particles and then subsequent averaging over the particles with volume V^p in the volume. Cast into an equation this reads

$$Q = \langle Q \rangle = \frac{1}{V} \sum_{p \in V} V^p Q^p \ , \tag{14}$$

where Q is the averaged macroscopic quantity and $Q^p = (1/V^p) \sum_{c=1}^{C^p} V_c Q^c$ is the pre-averaged particle quantity with the contact quantity Q^c and the volume associated to the contact, V_c. Here, the sub-script $p \in V$ denotes the particle-in-volume averaging procedure. The simplest macroscopic quantity is the volume fraction ν, as obtained from $Q^p = 1$.

3.1. The Fabric Tensor

For one particle with C^p contacts, the fabric tensor is defined as the sum, over all contacts, of the dyadic product formed by the normal vectors:

$$F^p_{\alpha\beta} = \sum_{c=1}^{C^p} n_\alpha n_\beta \ , \tag{15}$$

with the trace $\mathrm{tr}\boldsymbol{F}^p = F^p_{\gamma\gamma} = C^p$. Greek sub-scripts identify the tensor elements and the summation over equal indices is implied. In a large volume, with some distribution of particle radii, the relation between trace of fabric, density and average contact number C is, according to [34], $F_{\alpha\alpha} = g_2 \nu C$, with the average fabric, i.e. a contact number density,

$$F_{\alpha\beta} = \frac{1}{V} \sum_{p \in V} V^p \sum_{c=1}^{C^p} n_\alpha n_\beta \ , \tag{16}$$

and the correction factor

$$g_2 \approx 1 + \frac{\sqrt{3}}{\pi} \left(\frac{\overline{a^3}}{\overline{a}\,\overline{a^2}} - 1 \right) \ , \tag{17}$$

dependent on the first three moments of the size distribution $\overline{a^k}$ (with $k = 1, 2, 3$). In brief, g_2 corrects for the fact that the coordination number of different sized particles is proportional to their surface area, so that a monodisperse packing has $g_2 = 1$, whereas a polydisperse packing has $g_2 > 1$ with magnitude increasing with the width of the size distribution. Thus, a polydisperse packing has a higher contact number density than a monodisperse system of comparable density. It was shown recently that the correction, as tested for frictionless systems [34], is also relevant for frictional packings [14, 15].

3.2. *The Stress Tensor*

In the averaging volume V, one obtains the approximate (averaged) macroscopic stress from the dyadic product of the contact force, $\boldsymbol{f}^c$, and the (particle-center to contact) branch vector, $\boldsymbol{l}^c$,

$$\sigma_{\alpha\beta} = \frac{1}{V} \sum_{p \in V} \sum_{c=1}^{C^p} l_\alpha^c f_\beta^c \ , \tag{18}$$

Note that the particle volumes in Eq. (14) cancel due to the volume weight. Regarding the units, we interpret the stress as a potential energy density, with all contacts within V contributing. This is equivalent to the traditional definition of stress being the force per area on the surface of V.

3.3. *The elastic stiffness tensor*

The stiffness tensor relates the change of stress to an applied strain. For particles with branch vector length, $l = l^c$, and identical spring constants $k = k^c$, and $k^t = (k^t)^c$, one has:

$$C_{\alpha\beta\gamma\phi} = \frac{1}{V} \sum_{p \in V} \left(k \sum_{c=1}^{C} (2\,l^2) n_\alpha^c n_\beta^c n_\gamma^c n_\phi^c + k^t \sum_{c=1}^{C} (2\,l^2) n_\alpha^c t_\beta^c n_\gamma^c t_\phi^c \right) \ , \tag{19}$$

where the two contributions from normal and tangential springs can be examined separately. Note that this result can already be found in the literature [14, 35, 36] in similar form, however, we provide it here again, for the sake of completeness.

4. Averaged Quantities from simulations

As the essential step of a micro-macro transition, in the following, simulation results are presented for various side pressures p, different cohesion strength, k_c, and different friction coefficients, μ. Averages are performed such that parts of the system close to the walls are disregarded in order to avoid boundary effects. This means, that the averaging volume is about 64 per-cent of the total volume. A particle contact is taken into account for the average if the corresponding particle-center lies within the averaging volume V.

4.1. *Density dependence on isotropic confining pressure*

The first quantity of interest is the density (volume fraction), ν, as function of the side pressure p. After the preparation procedure (with $\mu = 0$ and $k_c = 0$), before deformation, the initial density and the pressure follow the relation

$$\frac{p}{p_0} = (\nu - \nu_0)^\alpha \ , \tag{20}$$

with $\alpha \approx 4/3$, $\nu_0 = 0.8361 \pm 0.0005$, and $p_0/k_2 = 1.16 \pm 0.05$. (Note that pressure p here is actually the product of the actual pressure and h, the height of the particles, and thus has units Nm^{-1}. Throughout the rest of the paper, pressure will be provided dimensionless, in units of $10^{-5}\,k_2$. This is obtained if the whole box with all particles is taken into account and the pressure is measured at the walls (normal wall force divided by wall-area). If only the central volume is taken into account, without the particles close to the wall, the relation is well fitted by the same curve with $\nu_0 = 0.848 \pm 0.002$, i.e. with a higher critical density ν_0, because the density close to the wall is reduced so that the density in the bulk is somewhat higher, and a slightly smaller exponent. In the limit $p \to 0$, the critical density ν_0 corresponds to the maximal possible packing density for rigid, friction- and cohesionless particles [37], and to the minimal density for which a stable, static packing is possible, for our friction- and cohesionless particles. Note however, that changing either the preparation procedure, the size distribution function, the friction coefficient or the cohesion, will affect the value of ν_0.

4.2. Isotropic and Deviatoric deformation

During the deformation as controlled by the top-wall, we report the volumetric strain, $2\epsilon_V = \Delta V/V$, and the deviatoric strain $\epsilon_D = (\varepsilon_{zz} - \varepsilon_{xx})/2$, with the vertical and horizontal strains, $\varepsilon_{zz} = 1 - z/z_0$, and $\varepsilon_{xx} = 1 - x/x_0$. Initially, one has $\epsilon_V \approx -(\varepsilon_{zz} + \varepsilon_{xx})/2 \approx m_V\,\varepsilon_{zz}$, and the system is compressed, $\epsilon_V < 0$, which is more pronounced for larger side pressures, see Fig. 3. From the initial slope m_V, one can obtain a Poisson ratio, $\nu_P = -\varepsilon_{xx}/\varepsilon_{zz} = 1 + m_V$, in the range $0.4 \le \nu_P \le 0.8$, decreasing with increasing pressure. The initial compression regime is followed by dilation (which sets in later for higher pressures), until a quasi-steady-state critical flow regime is reached, where the density is almost constant besides a weak tendency towards further dilation. The level of saturation decreases with increasing side pressure or, with other words, the critical state density increases with increasing side pressure.

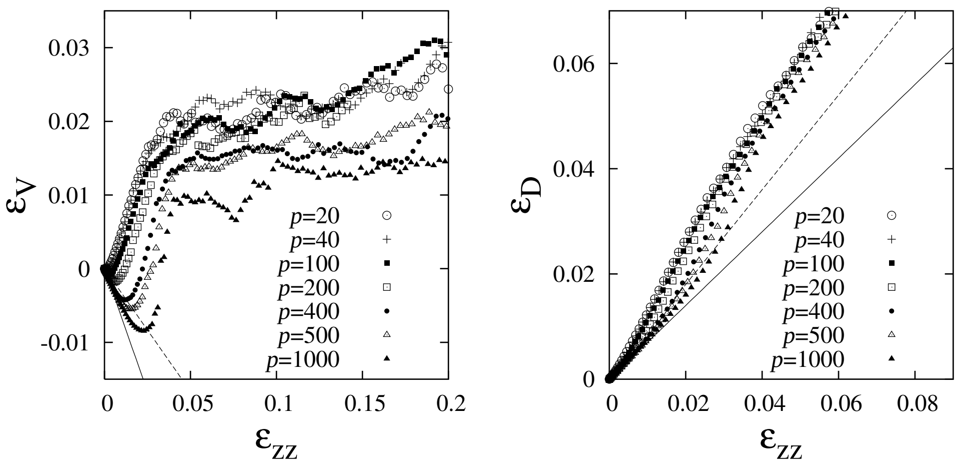

Figure 3. (Left) Volumetric strain, ε_V, (negative values mean compression) plotted against the vertical strain ε_{zz}. The dashed and solid lines correspond to $m_V\varepsilon_{zz}$, with $m_V = -0.2$ and $m_V = -0.6$, respectively. (Right) Deviatoric strain, ε_D, plotted against ε_{zz}, with the lines corresponding to $(1 + m_V/2)\,\varepsilon_{zz}$.

The deviatoric strain, ε_D, quantifies the amount of shear the medium undergoes in addition – and independently – of the compression/dilatancy. Initially, one has $\varepsilon_D \approx (1+2/m_V)\varepsilon_V$; the deviation from this asymptotic regime begins earlier for smaller side pressure. For larger deformations, the deviatoric strain becomes almost pressure independent, i.e. in the critical state flow regime, $\epsilon_V \approx$ const., the system undergoes only deviatoric strain.

An initially dilute granular medium (weak confining pressure) thus shows dilation almost from the beginning, whereas a denser granular material (under stronger confining pressure) can be compressed even further by the relatively strong external forces, before dilation starts. The range of density changes is $0.02 - 0.03$ in volume fraction, or volumetric stain, for the parameters used here. The material undergoes – due to the boundary conditions chosen – compression, dilation and volume conserving critical state flow. In addition, the system undergoes continuous shear, where the shear deformation is stronger and grows faster for smaller confining stress p, i.e. for larger p, the material is more resistant to shear.

4.3. Fabric Tensor

The fabric tensor is computed according to Eq. (16), and its isotropic and deviatoric contributions are displayed in Fig. 4. The isotropic contribution (the contact number density) is scaled by the prediction from [34], see Eq. (17), and the deviation from the prediction is between one to three percent, where the larger side pressure data are in better agreement (smaller deviation). Note that the correction due to the factor g_2 corresponds to about nine per-cent, and that the data are taken in the presence of friction, in contrast to the simulations by [34], a source of discrepancy, which accounts in our opinion for the remaining deviation.

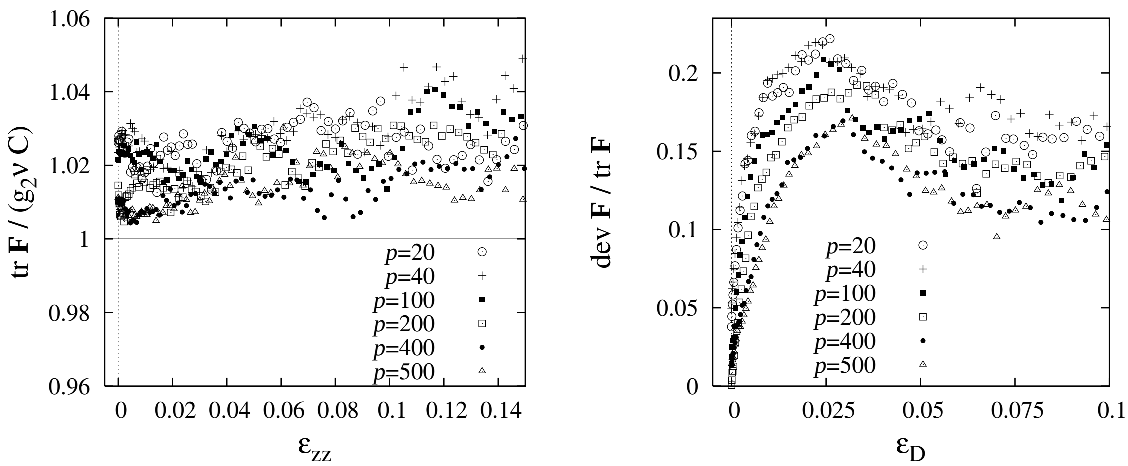

Figure 4. (Left) Quality factor for the trace of the fabric tensor scaled by the analytical prediction $g_2\nu C$ from [34], for different pressures p, as function of the vertical deformation. (Right) Deviatoric fraction of the fabric tensor from the same simulations plotted against the deviatoric strain.

The anisotropy of the granular packing is quantified by the deviatoric fabric, as displayed in its scaled form in Fig. 4. The anisotropy is initially of the order of a few percent at most – thus the initial configurations are not perfectly isotropic. With increasing deviatoric deformation, the anisotropy grows, reaches a maximum and then saturates on a lower level in the critical state flow regime. The scaled fabric grows faster for smaller side pressure and is also relatively larger for smaller p. The non-scaled fabric deviator, astonishingly, grows to values around $f_D^{\max}\mathrm{tr}\boldsymbol{F} \approx 0.56 \pm 0.03$, independently of the side pressures used here (data not shown, see [14, 15] for details). Using the definition $f_D := \mathrm{dev}\boldsymbol{F}/\mathrm{tr}\boldsymbol{F}$, the functional behavior,

$$\frac{\partial f_D}{\partial \varepsilon_D} = \beta_f \left(f_D^{\max} - f_D \right) \ , \tag{21}$$

was evidenced from simulations in Ref. [14], with $f_D^{\max}\mathrm{tr}\boldsymbol{F} \approx \mathrm{const.}$, and the deviatoric rate of approach $\beta_f = \beta_f(p)$, decreasing with increasing side pressure. The differential equation is solved by an exponential function that describes the approach of the anisotropy f_D to its maximal value, $1 - (f_D/f_D^{\max}) = \exp\left(-\beta_f \varepsilon_D\right)$, but not beyond.

4.4. Stress tensor

The behavior of the stress is displayed in Fig. 5, where the isotropic stress $(1/2)\mathrm{tr}\,\boldsymbol{\sigma}$ is plotted in units of p, and the deviatoric fraction is plotted in units of the isotropic stress. Note that the tangential forces do not contribute to the isotropic stress here since the corresponding entries in the averaging procedure compensate. From Fig. 5, we evidence that both normal contributions, the non-dimensional trace and the non-dimensional deviator behave similarly, independent of the side pressure: Starting from an initial value, a maximum is approached, where the maximum is only weakly dependent on p.

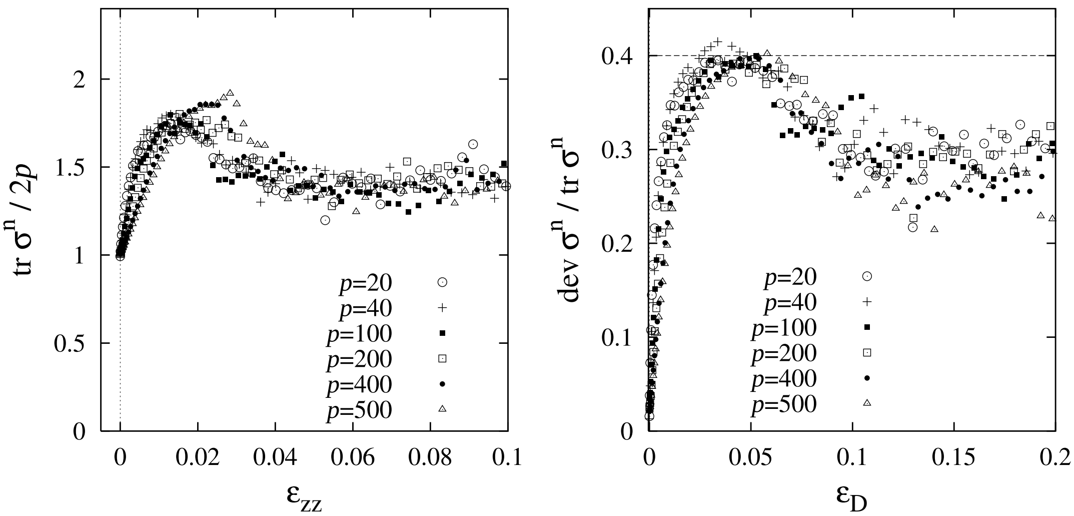

Figure 5. Non-dimensional stress tensor contributions for different p. The isotropic (Left) and the deviatoric fractions (Right) are displayed as functions of the vertical and deviatoric strain, respectively.

The increase of stress is faster for lower p. After the maximum is reached, the stresses decay and approach a smaller value in the critical state flow regime. Using the definitions $s_V := \mathrm{tr}\,\boldsymbol{\sigma}/(2p) - 1$ and $s_D := \mathrm{dev}\boldsymbol{\sigma}/\mathrm{tr}\boldsymbol{\sigma}$, the maximal (non-dimensional) isotropic and deviatoric stresses are $s_V^{\max} \approx 0.8 \pm 0.1$ and $s_D^{\max} \approx 0.4 \pm 0.02$, respectively, with a rather large error margin. The corresponding values at critical state flow are $s_V^c \approx 0.4 \pm 0.1$ and $s_D^c \approx 0.29 \pm 0.04$.

The evolution of the *deviatoric stress* fraction, s_D, as function of ε_D, is displayed in Fig. 5. Like the fabric, also the deviatoric stress exponentially approaches its maximum. This is described by the differential equation

$$\frac{\partial s_D}{\partial \varepsilon_D} = \beta_s \left(s_D^{\max} - s_D \right) \ , \tag{22}$$

where $\beta_s = \beta_s(p)$ is decaying with increasing p (roughly as $\beta_s \approx p^{-1/2}$). For more details on the deviatoric stress and also on the tangential contribution to the stress, see [14, 15].

4.5. Stiffness tensor

Given an arbitrary (small) deformation, the stiffness tensor relates the stress-changes to the deformation

$$\delta\sigma_{\alpha\beta} = C_{\alpha\beta\gamma\phi}\varepsilon_{\gamma\phi} + \delta\sigma_{\alpha\beta}^{struct.} \ , \tag{23}$$

where the first term corresponds to the elastic (reversible) structural anisotropy, and the second term contains the stress changes due to a change in structure. The stiffness tensor entries $C_{\alpha\beta\gamma\phi}$ were discussed in detail in [14, 15], where it was concluded that there are typically only three different moduli $C_1 := C_{xxxx}$, $G := C_{xxzz} = C_{zzxx}$, and $C_2 := C_{zzzz}$ due to normal forces, in the coordinate system of the biaxial box. Tensor entries with an odd number of indices are practically zero. Also the stiffness entries due to the tangential forces are related to these three moduli [14], but will not be discussed in detail here.

In the following, we recall Ref. [14, 15], and rewrite Eq. (23) in terms of $\delta\sigma_V$, $\delta\sigma_D$, ϵ_V, and ε_D, where the indices V and D denote the isotropic and the deviatoric contributions, respectively. Note that $\epsilon_V = -\varepsilon_V/2$ is used here for convenience. Since in the biaxial box system, the eigensystem of the tensors is oriented according to the wall geometry, a scalar formulation is possible for the isotropic stress:

$$\delta\sigma_V = \delta\sigma_{\alpha\alpha}/2 = E\left(\epsilon_V + \frac{A}{E}\,\varepsilon_D\right) + \delta\sigma_{\alpha\alpha}^{struct.}/2 \ , \tag{24}$$

with $\epsilon_V = (1/2)(\varepsilon_{xx}+\varepsilon_{zz})$, $\varepsilon_D = (1/2)(\varepsilon_{zz}-\varepsilon_{xx})$, and the isotropic compression modulus $E = (C_1 + C_2 + 2G)/2$ that relates an isotropic deformation to an isotropic stress-change, and the anisotropic modulus $A = (C_2 - C_1)/2$ that relates isotropic (deviatoric) deformations, to deviatoric (isotropic) stress-changes. For the deviatoric stress one has:

$$\delta\sigma_D = \delta\left(\sigma_{zz} - \sigma_{xx}\right)/2 = E\left(\frac{A}{E}\,\epsilon_V + \frac{B}{E}\,\varepsilon_D\right) + \delta\sigma_D^{struct.} \ ,$$

with the deviatoric shear modulus $B = (C_1 + C_2 - 2G)/2 = E - 2G$ that relates an anisotropic deformation to an anisotropic stress-change. Thus the anisotropic, elastic material behavior is described (in the biaxial cartesian coordinates) by the compression modulus E and the two dimensionless numbers A/E and B/E, which quantify anisotropy and deviatoric shear strength, respectively.

From the simulations presented in the previous subsections, the moduli are plotted in Fig. 6. We observe first, that the modulus E is proportional to the trace of the fabric tensor, $E \propto \mathrm{tr}\boldsymbol{F}$ (data not shown). Plotted against the volumetric deformation, we observe, that E increases with pressure from about $0.78k_n$ to $1.05k_n$, both in the initial state and the critical flow state. The initial compression leads to a temporary increase of stiffness in the range from one to ten per-cent, an effect which is more pronounced for larger confining pressure.

The shear stiffness ratio B/E starts at a value close to 0.5 and rapidly drops by 6-8 per-cent, then increases a few per-cent and levels out at values around 0.475 ± 0.010 in the critical state regime.

The anisotropic stiffness ration A/E increases from zero to peak values from 0.16 to 0.22, for small deviatoric strain – like the deviatoric fraction of the fabric tensor. After the peak, A/E decays and reaches values between 0.1 and 0.17. The anisotropic modulus A/E, related to the isotropic modulus, becomes somewhat less important with increasing confining pressure.

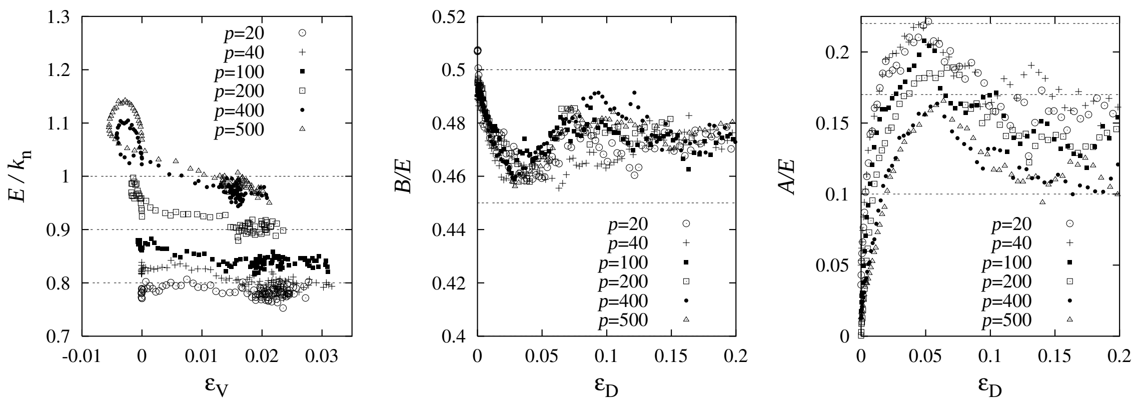

Figure 6. (Left) Isotropic modulus E, scaled by k_n, plotted as function of ε_V, (Middle) Shear modulus ratio, B/E, plotted as function of ε_D, and (Right) Anisotropic modulus ratio, A/E, plotted as function of ε_D.

4.6. Variation of the microscopic cohesion

Two series of simulations with varying cohesion strength, k_c, and vanishing friction, $\mu = 0$, are performed at initial confining pressures $p = 500$ and $p = 100$, see Figs. 7 and 8. For small strain ε_{zz}, the material is compressed, as indicated by negative ε_V, extending to larger (negative) values for stronger cohesion k_c and larger external pressure p. The inital slope, $m_V \approx -0.31$, can be related to the Poisson-ratio $\nu_P = 1 + m_V \approx 0.69$, and appears to be independent of both cohesion strength and pressure – in the absence of friction.

When the upper wall continues to move, dilatancy is evidenced at ε_{zz}-values between one and two per-cent for large external stress, but already for much smaller strain if the external pressure is smaller. The positive slope can be related to a dilatancy angle [10, 38], as used in some material models. The onset of dilatancy typically takes place before the maximum vertical stress is achieved and thus before the failure of the material. The transition from the compressive to the dilatant regime is delayed to larger strain by stronger cohesion and stronger external pressure.

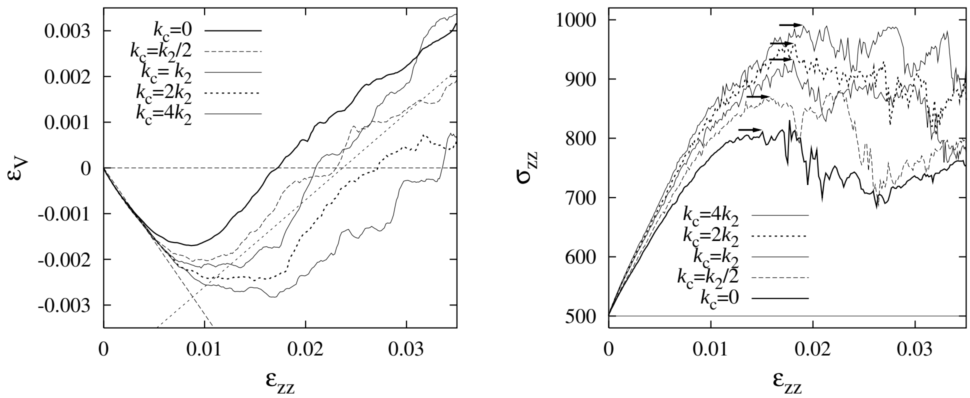

Figure 7. Simulation results from runs with $k_1 = k_2/2$, and different cohesion strength k_c, as given in the inset for $p = 500$. (Left) Volume change is plotted against ε_{zz}, and the straight lines indicate the slopes -0.32 and $+0.19$. (Right) Vertical stress σ_{zz} plotted against ε_{zz}; the arrows indicate the peak-stress.

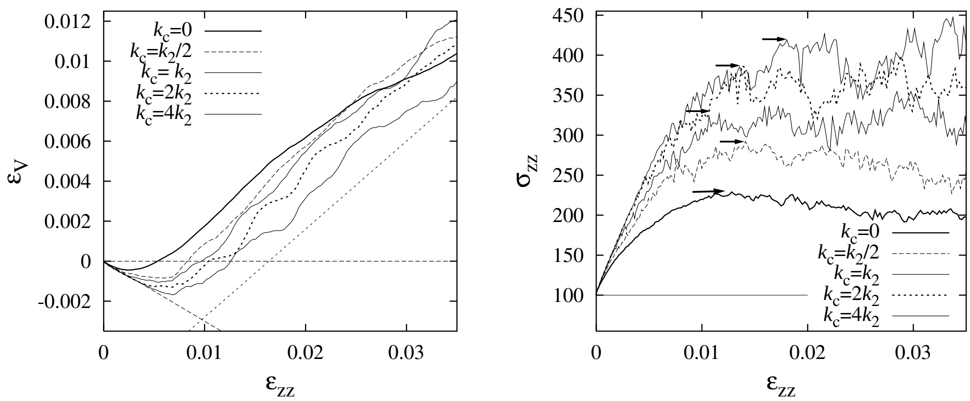

Figure 8. The same as in Fig. 7, only here $p = 100$, and the straight lines indicate the slopes -0.30 and $+0.44$.

From the initial slope of the stress-strain curves, one could extract a modulus of the material, increasing with increasing strength of cohesion. After failure (see figures), softening is obtained for large p and weak cohesion. The critical state regime is here also accompanied by strong fluctuations. The maximum stress from each simulation is indicated by an arrow in the figures. For more details concerning the rate-dependence and the relaxation rates of these simulations, see Ref. [10].

4.7. Yield-Stress and macroscopic cohesion

The yield-stresses from Figs. 7 and 8 are combined in Fig. 9 as Mohr-circles. Each set of Mohr circles corresponds to a fixed external pressure p and different circles correspond to different $k_c/k_2 = 0$, $1/2$, 1, 2, and 4, from the smallest to the largest circle, respectively. The tangent to a pair of circles with the same cohesion strength is plotted as a dotted line for all pairs. The slope of the lines is $\tan\phi \approx 0.23$ corresponding to an internal friction angle $\phi \approx 13^o$. Due to the absence of any microscopic friction in the model, the macroscopic friction, $\tan\phi$, has to be caused by the geometry of the packing which causes a shear resistance due to inter-locked particles.

The macroscopic *cohesion* c of the material can be obtained as the point of intersection of the dashed line and the zero vertical axis, as detailed in [10], see Fig. 9. We note that c is not linear in k_c, but saturates after a strong increase for small k_c. The solid line gives the maximal attractive force, f_{min}, see subsection 2.1.2, which behaves analogously, thus relating the macroscopic cohesion, c, to the microscopic attractive force, as defined in the contact model.

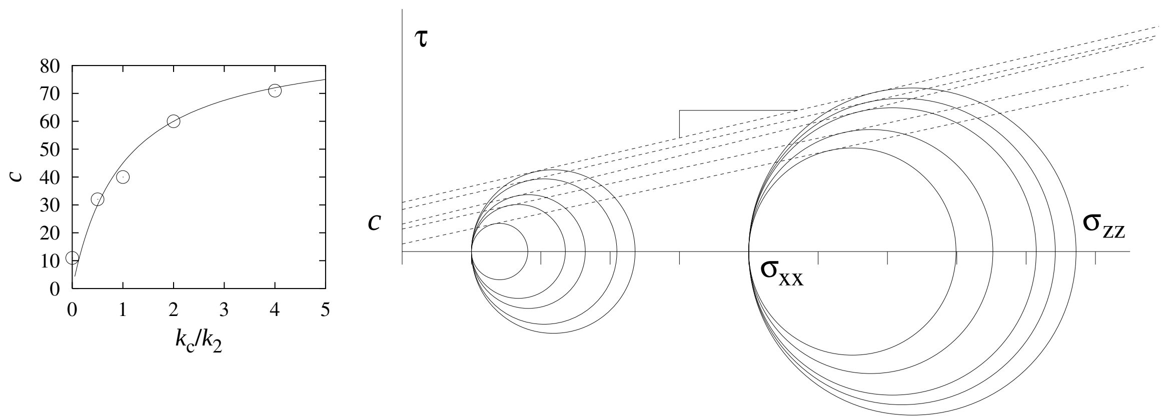

Figure 9. Yield surface for simulations with $\mu = 0$ and varying k_c. (Left) Macroscopic cohesion c as function of the cohesion strength k_c, with the maximum attractive force $c \propto (k_2 - k_1)/(k_2 + k_c)$ given as solid line. (Right) Mohr circles at failure, for the simulations in Figs. 7 and 8. The left end of the circle corresponds to the fixed pressure p, the right end to the vertical pressure σ_{zz} at failure. The angle indicates a slope of about 0.23.

4.8. Variation of the friction coefficient

In the final set of simulations, we restrict ourselves to cohesionless material, $k_c = 0$, but here the microscopic coefficient of friction μ is varied. In Fig. 10, volumetric strain and deviatoric stress are plotted for simulations with $p = 200$ and different μ.

The volumetric strain shows compression (decrease), dilatancy (increase) and critical state behavior (constant), like in the figures above. Here we note that the rate and the amount of dilatancy increases strongly with increasing μ, from very small values for $\mu = 0$ up to volume changes of around two per-cent for $\mu = 0.5$. The deviatoric stress increases, then the slope gradually decreases (softening), until the stress reaches its maximum (peak yield stress). After the peak, further softening/weakening behavior (with negative slope) is followed by a constant, strongly fluctuating stress for larger deformations, in the critical state flow regime. Peak stress, critical state stress and also the magnitude of softening increase with increasing μ.

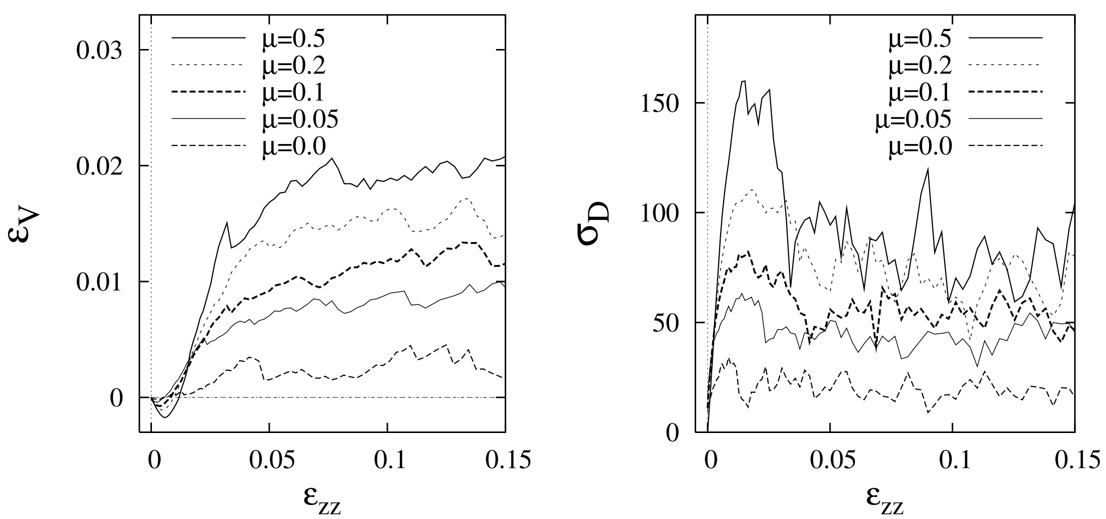

Figure 10. (Left) Volumetric strain as function of vertical strain from simulations with $p = 200$ and different coefficients μ. (Right) Anisotropic stress as function of vertical strain from the same simulations.

For $\mu = 0.5$, somewhat softer particles, and larger viscosity, we show in Fig. 11 (Left) that the yield surface is approximately linear with a slope of 0.588. Given this linearity together with the linearity for $\mu = 0$, one can extract the macroscopic friction coefficients, $\tan \phi$, from the peak stresses of a single simulation, as shown in Fig. 10, using the relation

$$\sin \phi = \frac{\sigma_{zz} - \sigma_{xx}}{\sigma_{zz} + \sigma_{xx}} \ . \tag{25}$$

Data for different simulations with different initial conditions and different deformation rates t_s are shown in Fig. 11 (Right). Macroscopic friction is evidenced already for vanishing microscopic friction, increasing with μ. For larger μ values, the macroscopic friction bends and seems to saturate. Simulations with comparatively large viscosity and faster compression lead to larger friction. Thus it is important to deform the sample very slowly in order to obtain quasi-static results. Also the initial condition affects the result, i.e. simulations prepared with strong friction – when compressed with smaller friction – first collapse and later lead to slightly larger peak friction.

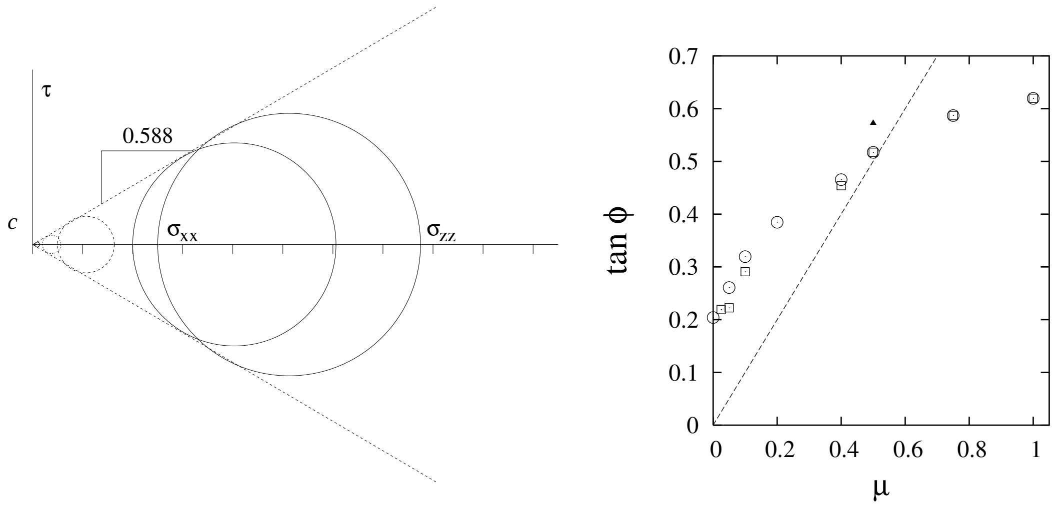

Figure 11. (Left) Mohr circle representation of the flow function at peak stress from simulations with different pressure and $\mu = 0.5$, and fast strain rate $t_s \approx 0.5$ s. (Right) Macroscopic friction coefficient as function of the microscopic friction for fast (solid symbol) and slow strain rates $t_s \approx 10$ s (open symbols). Simulations were started from a configuration prepared with $\mu = 0$ (squares) and with $\mu = 0.5$ (circles).

4.9. Summary of macroscopic material parameters

From the simulation data, it is possible to obtain the following material parameters, as based on an isotropy/homogeneity assumption:

(i) The initial slope of the volumetric strain allows to determine the Poisson ratio, dependent on the side stress p and microscopic friction μ, but almost independent of cohesion strength k_c.

(ii) The slope of the volumetric strain in the dilatancy regime (about $+0.4$ without friction and $p = 100$, about $+0.2$ without friction and $p = 500$, and up to about $+0.8$ with strong friction, but without cohesion) is related to the dilatancy angle. Dilatancy is hindered by large side stresses, but much stronger dilatancy is evidenced in the presence of strong friction. Cohesions seemingly does not affect the dilatancy.

(iii) The initial slope of the pressure, when plotted against the volumetric strain, is related to the macroscopic bulk modulus E, which like the shear and the anisotropic moduli, B and A, can be also obtained from the stiffness tensor. The shear modulus is almost constant $B \approx E/2$ for the boundary conditions used here, while the anisotropic modulus increases from zero to a maximal value, and shows softening and critical state flow behavior for larger deformations.

(iv) The peak (yield) stress is related to the flow function of the material. Also in the absence of microscopic friction, there is a macroscopic friction due to geometrical, structural effects. With increasing microscopic friction, also the macroscopic friction increases, until it tends to saturate for values $\mu > 1$. We remark that these results are sensitive to details of sample preparation and parameter choice.

As a final remark, we note that some of the micro-macro transition results depend slightly on the averaging procedure and averaging volume.

5. Summary and Conclusion

In summary, a set of DEM simulations was presented, and several macroscopic material parameters like, e.g., the macroscopic cohesion, the friction angle, and three bulk moduli, were extracted from the simulation data with cohesion (no friction) and with friction (no cohesion), for different confining pressures. The macroscopic cohesion could be related to the minimal force (the maximal attractive force) in the microscopic contact model. The macroscopic friction angle is not directly related to the microscopic friction angle, due to geometrical interlocking and dilatancy effects; furthermore, the macroscopic friction seems to saturate for large microscopic friction coefficients.

From the presented data, it can be concluded that there are basically only three different quantities in the stiffness tensor, scaling with the microscopic spring stiffness used for the simulation, which quantify the stress response of a static granular packing – disregarding changes of the structure. The bulk modulus E slightly increases with density and confining pressure. The shear modulus B is almost invariant relative to E, and the anisotropic modulus A shows the largest variation from the initial isotropic state to peak stress, and then decays to the critical state flow value. The magnitude of the maximum of A/E is inverse proportional to the confining pressure.

Stress responses are proportional to the isotropic fabric F_V in magnitude, because this is proportional to the isotropic modulus E. The deviatoric fraction of the fabric behaves like the anisotropic modulus A/E. For both deviator fabric and stress, an exponential approach to the maximal value was observed, with rate of approach increasing with decreasing confining stress.

Together with shear band localization, also the role of particle rotations is an open issue, as related to micro-polar constitutive models: In both simulation and experiment, rotations are active in the shear band. Local averaging in smaller averaging volumes (areas), the corresponding parameter identification, and the micro-macro-transition for anisotropic micro-polar continuum models is a challenge for the future, like the implementation and simulation of experimentally determined force-laws in more realistic three-dimensional systems.

Acknowledgments

We thank E. Clément, J. Jenkins, N. P. Kruyt, M. Madadi, F. Nicot, R. G. Rojo, C. Thornton, J. Tomas, and R. Tykhoniuk for helpful discussions and acknowledge the support of the Deutsche Forschungsgemeinschaft (DFG). This work is part of the research programme of the Stichting voor Fundamenteel Onderzoek der Materie (FOM), financially supported by the Nederlandse Organisatie voor Wetenschappelijk Onderzoek (NWO) and the Stichting Shell Research.

References

[1] H. J. Herrmann, J.-P. Hovi, and S. Luding, editors. *Physics of dry granular media - NATO ASI Series E 350*, Dordrecht, 1998. Kluwer Academic Publishers.

[2] P. A. Vermeer, S. Diebels, W. Ehlers, H. J. Herrmann, S. Luding, and E. Ramm, editors. *Continuous and Discontinuous Modelling of Cohesive Frictional Materials*, Berlin, 2001. Springer. Lecture Notes in Physics 568.

[3] Y. Kishino, editor. *Powders & Grains 2001*, Rotterdam, 2001. Balkema.

[4] C. S. Chang and L. Ma. A micromechanical-based micropolar theory for deformation of granular solids. *Int. J. of Solids and Structures*, 21(1):67–86, 1991.

[5] M. Babić. Average balance equations for granular materials. *Int. J. Engng. Sci.*, 35(5):523–548, 1997.

[6] K. Bagi. Microstructural stress tensor of granular assemblies with volume forces. *J. Appl. Mech.*, 66:934–936, 1999.

[7] Masanobu Oda and Kazuyoshi Iwashita. Study on couple stress and shear band development in granular media based on numerical simulation analyses. *Int. J. of Enginering Science*, 38:1713–1740, 2000.

[8] J. P. Bardet and I. Vardoulakis. The asymmetry of stress in granular media. *Int. J. of Solids and Structures*, 38(2):353–367, 2001.

[9] A. S. J. Suiker, A. V. Metrikine, and R. de Borst. Comparions of wave propagation characterisitcs of the cosserat continuum model and corresponding discrete lattice models. *Int. J. of Solids and Structures*, 38:1563–1583, 2001.

[10] S. Luding and H. J. Herrmann. Micro-macro transition for cohesive granular media. in: Bericht Nr. II-7, Inst. für Mechanik, Universität Stuttgart, S. Diebels (Ed.), 2001.

[11] J. P. Peters and D. A. Horner. Errors of scale in discrete element computations. In K. Cook and R. P. Jensen, editors, *Discrete Element Methods: Numerical Modeling of Discontinua*, pages 56–67, Santa Fe, 2002. ASCE.

[12] I. Goldhirsch and C. Goldenberg. On the microscopic foundations of elasticity. *Eur. Phys. J. E*, 9(3):245–251, 2002.

[13] N. P. Kruyt. Statics and kinematics of discrete cosserat-type granular materials. *Int. J. of Solids and Structures*, 40(3):511–534, 2003.

[14] S. Luding. Micro-macro transition for anisotropic, frictional granular packings. *Int. J. Sol. Struct.*, 41:5821–5836, 2004.

[15] S. Luding. Micro-macro models for anisotropic granular media. In P. A. Vermeer, W. Ehlers, H. J. Herrmann, and E. Ramm, editors, *Modelling of Cohesive-Frictional Materials*, pages 195–206, Leiden, Netherlands, 2004. A. A. Balkema.

[16] C. Thornton. Numerical simulations of deviatoric shear deformation of granular media. *Géotechnique*, 50(1):43–53, 2000.

[17] P. A. Cundall and O. D. L. Strack. A discrete numerical model for granular assemblies. *Géotechnique*, 29(1):47–65, 1979.

[18] Y. M. Bashir and J. D. Goddard. A novel simulation method for the quasi-static mechanics of granular assemblages. *J. Rheol.*, 35(5):849–885, 1991.

[19] S. van Baars. *Discrete Element Analysis of Granular Materials.* PhD thesis, Technische Universiteit Delft, Delft, Nederlands, 1996.

[20] C. Thornton and S. J. Antony. Quasi-static deformation of a soft particle system. *Powder Technology*, 109(1-3):179–191, 2000.

[21] N. P. Kruyt and L. Rothenburg. Statistics of the elastic behavior of granular materials. *Int. J. of Solids and Structures*, 38:4879–4899, 2001.

[22] S. Luding, R. Tykhoniuk, and J. Tomas. Anisotropic material behavior in dense, cohesive powders. *Chem. Eng. Technol.*, 26(12):1229–1232, 2003.

[23] S. Luding. Molecular dynamics simulations of granular materials. In H. Hinrichsen and D. E. Wolf, editors, *The Physics of Granular Media*, pages 299–324, Weinheim, Germany, 2004. Wiley VCH.

[24] S. Luding, K. Manetsberger, and J. Müllers. A disrete model for long time sintering. *J. Mech. Phys. Sol.*, 53(2):455–491, 2005.

[25] S. Luding. Collisions & contacts between two particles. In H. J. Herrmann, J.-P. Hovi, and S. Luding, editors, *Physics of dry granular media - NATO ASI Series E350*, page 285, Dordrecht, 1998. Kluwer Academic Publishers.

[26] O. R. Walton and R. L. Braun. Viscosity, granular-temperature, and stress calculations for shearing assemblies of inelastic, frictional disks. *Journal of Rheology*, 30(5):949–980, 1986.

[27] Jürgen Tomas. Particle adhesion fundamentals and bulk powder consolidation. *KONA*, 18:157–169, 2000.

[28] C. Y. Zhu, A. Shukla, and M. H. Sadd. Prediction of dynamic contact loads in granular assemblies. *J. of Applied Mechanics*, 58:341, 1991.

[29] M. H. Sadd, Q. M. Tai, and A. Shukla. Contact law effects on wave propagation in particulate materials using distinct element modeling. *Int. J. Non-Linear Mechanics*, 28(2):251, 1993.

[30] L. Brendel and S. Dippel. Lasting contacts in molecular dynamics simulations. In H. J. Herrmann, J.-P. Hovi, and S. Luding, editors, *Physics of Dry Granular Media*, page 313, Dordrecht, 1998. Kluwer Academic Publishers.

[31] S. Luding, E. Clément, A. Blumen, J. Rajchenbach, and J. Duran. Anomalous energy dissipation in molecular dynamics simulations of grains: The "detachment effect". *Phys. Rev. E*, 50:4113, 1994.

[32] S. Luding, E. Clément, A. Blumen, J. Rajchenbach, and J. Duran. The onset of convection in molecular dynamics simulations of grains. *Phys. Rev. E*, 50:R1762, 1994.

[33] M. Lätzel, S. Luding, and H. J. Herrmann. Macroscopic material properties from quasi-static, microscopic simulations of a two-dimensional shear-cell. *Granular Matter*, 2(3):123–135, 2000. cond-mat/0003180.

[34] M. Madadi, O. Tsoungui, M. Lätzel, and S. Luding. On the fabric tensor of polydisperse granular media in 2d. *Int. J. Sol. Struct.*, 41(9-10):2563–2580, 2004.

[35] C.-L. Liao and T.-C. Chang. A generalized constitutive relation for a randomly packed particle assembly. *Computers and Geotechnics*, 20(3/4):345–363, 1997.

[36] N. P. Kruyt and L. Rothenburg. Statistical theories for the elastic moduli of two-dimensional assemblies of granular materials. *Int. J. of Engineering Science*, 36:1127–2242, 1998.

[37] S. Luding. Liquid-solid transition in bi-disperse granulates. *Advances in Complex Systems*, 4(4):379–388, 2002.

[38] P. A. Vermeer. Non-associated plasticity for soils, concrete and rock. In H. J. Herrmann, J.-P. Hovi, and S. Luding, editors, *Physics of dry granular media - NATO ASI Series E350*, page 163, Dordrecht, 1998. Kluwer Academic Publishers.